Wave Attenuation Through an Arctic Marginal Ice Zone on 12 October 2015: 1. Measurement of Wave Spectra and Ice Features From Sentinel 1A

J. E. Stopa, Fabrice Ardhuin, Jim Thomson, Madison M. Smith, Alison Kohout, Martin Doble, Peter Wadhams

AGU100 ADVANCING EARTH AND SPACE SCIENCE

JGR

Journal of Geophysical Research: Oceans

RESEARCH ARTICLE

10.1029/2018JC013791

Special Section:
Sea State and Boundary Layer Physics of the Emerging Arctic Ocean

Wave Attenuation Through an Arctic Marginal Ice Zone on 12 October 2015: 1. Measurement of Wave Spectra and Ice Features From Sentinel 1A

J. E. Stopa[1], F. Ardhuin[1], Jim Thomson[2], Madison M. Smith[2], Alison Kohout[3], Martin Doble[4], and Peter Wadhams[5]

[1]Univ. Brest, CNRS, IRD, Ifremer, Laboratoire d'Océanographie Physique et Spatiale, IUEM, Brest, France, [2]Applied Physics Laboratory, University of Washington, Seattle, WA, USA, [3]National Institute of Water and Atmospheric Research, Christchurch, New Zealand, [4]Polar Scientific, Ltd., Appin, UK, [5]Cambridge Polar Consultants Ltd., Cambridge, UK

Key Points:
- Wave spectra are retrieved from SAR Sentinel-1A across 400 km of the marginal ice zone
- Strong wave attenuation is observed just inside the ice edge, with weaker decay further into the ice
- The transition in wave attenuation could be related to the observed changes in young sea ice conditions

Correspondence to:
J. E. Stopa,
justin.stopa@ifremer.fr

Citation:
Stopa, J. E., Ardhuin, F., Thomson, J., Smith, M. M., Kohout, A., Doble, M., et al. (2018). Wave attenuation through an Arctic marginal ice zone on 12 October 2015: 1. Measurement of wave spectra and ice features from Sentinel 1A. *Journal of Geophysical Research: Oceans*, *123*, 3619–3634. https://doi.org/10.1029/2018JC013791

Received 12 JAN 2018
Accepted 23 APR 2018
Accepted article online 30 APR 2018
Published online 20 MAY 2018

Abstract A storm with significant wave heights exceeding 4 m occurred in the Beaufort Sea on 11–13 October 2015. The waves and ice were captured on 12 October by the Synthetic Aperture Radar (SAR) on board Sentinel-1A, with Interferometric Wide swath images covering 400 × 1,100 km at 10 m resolution. This data set allows the estimation of wave spectra across the marginal ice zone (MIZ) every 5 km, over 400 km of sea ice. Since ice attenuates waves with wavelengths shorter than 50 m in a few kilometers, the longer waves are clearly imaged by SAR in sea ice. Obtaining wave spectra from the image requires a careful estimation of the blurring effect produced by unresolved wavelengths in the azimuthal direction. Using in situ wave buoy measurements as reference, we establish that this azimuth cutoff can be estimated in mixed ocean-ice conditions. Wave spectra could not be estimated where ice features such as leads contribute to a large fraction of the radar backscatter variance. The resulting wave height map exhibits a steep decay in the first 100 km of ice, with a transition into a weaker decay further away. This unique wave decay pattern transitions where large-scale ice features such as leads become visible. As in situ ice information is limited, it is not known whether the decay is caused by a difference in ice properties or a wave dissipation mechanism. The implications of the observed wave patterns are discussed in the context of other observations.

Plain Language Summary Our work entitled "Wave attenuation through an Arctic marginal ice zone on 12 October 2015. 1. Measurement of wave spectra and ice features from Sentinel-1A," uses a newly developed method to extract wave spectra from radar imagery over sea ice. This is possible since the sea ice rapidly removes the short waves which usually distort the radar imagery. We are able to estimate thousands of wave spectra across several hundred kilometers at kilometer-scale resolution for the first large-scale view of wave attenuation across the marginal ice zone. Our results show a unique wave attenuation pattern described by a piecewise exponential decay that changes by a factor of 10. The transition between the different wave attenuation regions occurs near a change in sea ice conditions we estimate from the SAR backscatter. This suggests the wave-ice interaction mechanisms are indeed changing over these large scales.

1. Introduction

To quantify global budgets of heat and momentum, it is essential to understand the exchanges between the atmosphere, ocean, and ice. Wave action is typically not considered in coupled numerical models near and within the marginal ice zone (MIZ) (Marshall & Zanna, 2014; Stroeve et al., 2007; Turner et al., 2013). Wave action modulates and possibly enhances exchanges through ice breakup (Kohout et al., 2014), upper ocean mixing (Smith et al., 2018), and wave-induced sea ice drift (Masson, 1991; Stopa et al., 2018). The intensity and spatial extent of these processes is defined by the wave attenuation in the ice. In this study, we explore wave attenuation during a particular storm that occurred in the Beaufort Sea on 11–13 October 2015.

Following a special request from a European Union funded project, the European Space Agency programmed a few acquisitions of the synthetic aperture radar (SAR) on Sentinel-1A (S1A) in Interferometric

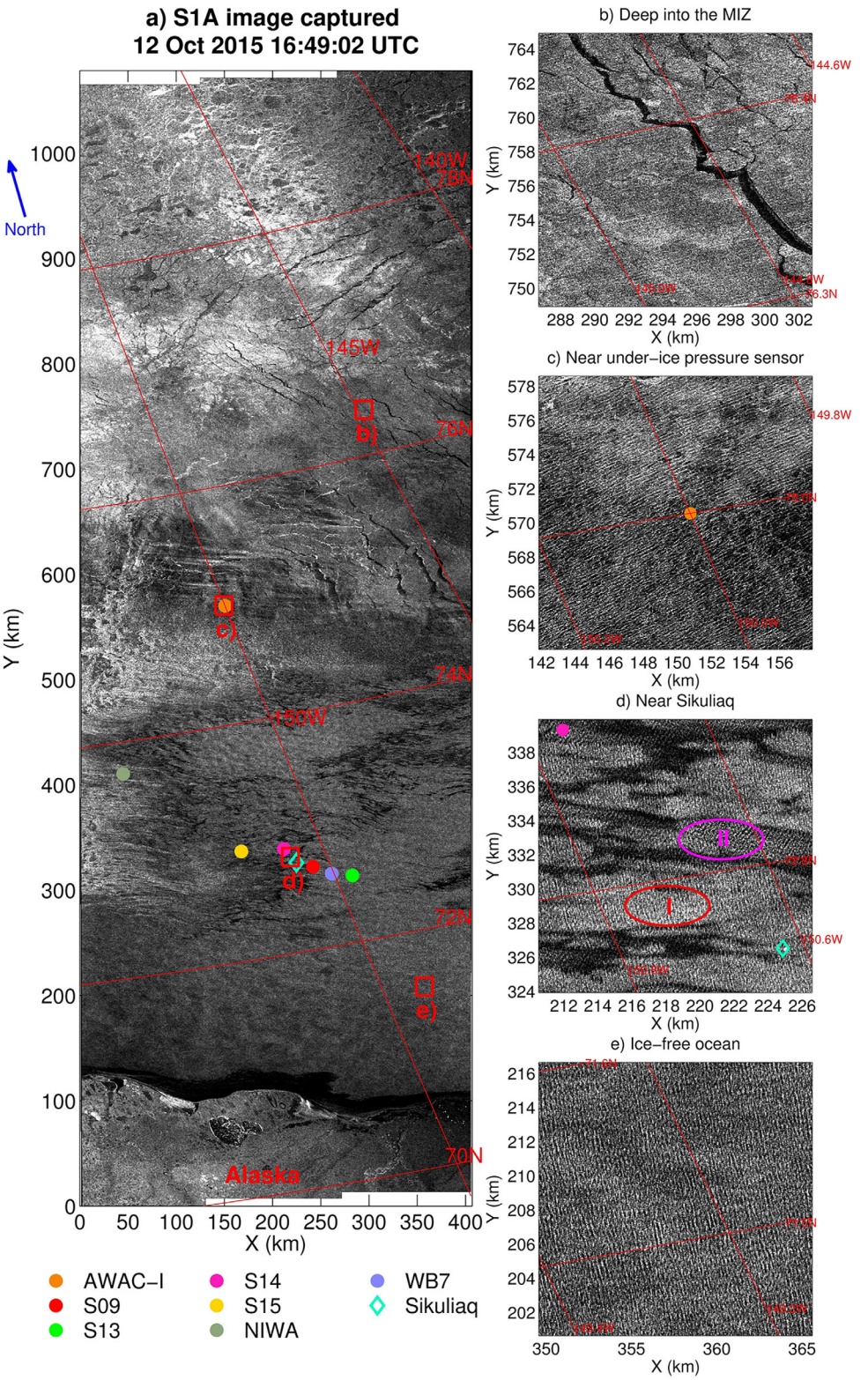

Figure 1. Sentinel-1A roughness image acquired 12 October 2015 16:50:00 UTC in a descending pass. (a) The entire image overview starting roughly 1,100 km from the North coast of Alaska crossing the Beaufort-Chuckchi Sea. (b) A region deep into the sea ice where leads and waves are observed. (c) The location where the under-ice acoustic Doppler profile was deployed and waves are observed. (d) A region close to the Sikuliaq near the ice edge were drifting buoys are deployed. (e) An ice-free region. A full resolution image can be visualized interactively at http://tiny.cc/S1AOct12.

wide swath (IW) mode (see also Ardhuin et al., 2017a). One of these S1A IW images was acquired on 12 October 2015 at 16:50 UTC, and is shown in Figure 1. The acquisition covers 400 × 1,100 km at approximately 10 m resolution extending across the marginal ice zone (MIZ) from the North coast of Alaska located at 70°N to 80°N. At the time of the satellite overpass, field operations were underway from the Research Vessel Sikuliaq (Thomson et al., 2017). This includes a deployed array of drifting wave buoys which were located near the ice edge within the MIZ as illustrated in Figure 1a. One of the main motivations of the present study comes from the exceptional large-field of view and coincidence of a large wave event.

The wave behavior and ice conditions near the ice edge during this event have been carefully investigated by Rogers et al. (2016), and Cheng et al. (2017). Here we focus instead on wave penetration further into the ice (>100 km from the ice edge). Even several hundred kilometers from the ice edge (Figure 1b), ocean waves signatures are visible on the S1A image. In situ wave measurements from buoys provide highly valuable information, but have only sparse spatial coverage. Wave attenuation estimated from pairs of sensors can miss important spatial variability. Using remote sensing from satellites is highly advantageous because it is possible to characterize wave processes throughout the MIZ, including regions far from the ice edge. Therefore, our goal is to estimate and describe the wave attenuation across the entire MIZ.

Previous studies of wave attenuation in the MIZ have combined in situ observations, remote sensing, and theoretical formulations. Wadhams et al. (1988) was the first comprehensive study that described wave attenuation from in situ observations using multiple experiments in the Bering and Greenland Seas. More recently there have been studies exploring the relative importance of scattering versus attenuation processes using in situ observations (Ardhuin et al., 2016). Liu et al. (1992) used remote sensing observations from SAR which were collected from an aircraft during the LIMEX 1987 and 1989 experiments near Newfoundland, Canada. They estimated wave attenuation and compared results to the decay model of Liu and Mollo-Christensen (1988). Recent theoretical wave studies have considered both wave attenuation and scattering processes (Montiel et al., 2016; Sutherland et al., 2017). For a review of theoretical considerations of wave propagation in sea ice (see Squire, 2007). Most studies have reported exponential wave attenuation, with varying decay coefficients, which are presumed to depend on ice conditions and wave frequency. The relationship of decay coefficients with ice conditions and wave frequency will be explored in this study especially at larger spatial scales where it is certain that ice conditions change.

SAR data have been widely used to measure wavelengths and directions in the ice (e.g., Gebhardt et al., 2016; Shulz-Stellenfleth & Lehner, 2002). Additionally, it is possible to estimate wave heights assuming that the patterns in the SAR image are dominated by the velocity bunching effect, as illustrated in Figure 2. The scatterers in the SAR image are displaced in the azimuthal direction as a function of their Doppler velocity. This results in bright intensity lines located in the regions of vertical velocity convergence. In the open ocean, the velocity bunching associated with the shorter waves of the spectrum produce a strong blurring that leads to an azimuthal cutoff effect (Kerbaol et al., 1998). In practice, the azimuth cutoff represents the minimum detectable wavelength by the SAR. As a result, the wave spectrum is attenuated by a factor $\exp\left(-(k_y\lambda_c/\pi)^2\right)$ where k_y is the wave number in the azimuth direction and λ_c is the cutoff wavelength. However, when the orbital velocity is sufficiently small, this velocity bunching can be constructive, thanks to the presence of sea ice that damps the shorter ocean waves (Alpers & Rufenach, 1979; Ardhuin et al., 2015; Lyzenga et al., 1985). In these conditions, the wave directional spectra can be retrieved from SAR imagery (Ardhuin et al., 2017a). On Sentinel-1, waves of period 10 s with significant wave height as low as 0.5 m produce an easily detectable 2 dB difference between bright and dark lines in the radar cross sections (Ardhuin et al., 2015). Important adaptations of the SAR inversion were required to flag the wave spectra contaminated by ice features, and estimate the azimuthal cutoff from the SAR image. With these adaptations, we estimate wave spectra across the S1A image in Figure 1 and measure wave attenuation.

The manuscript is organized as follows. In section 2, we describe the environmental conditions, our data sets, and the inversion method used to extract wave spectra from SAR imagery. The sea ice features result in a large range of backscatter values which makes retrieval of quantitative information challenging. Thus, section 3 is dedicated to describing the specific procedures implemented to flag subimages influenced by ice features. This includes a comparison of the orbital wave velocities with SAR estimates through the azimuth cutoff. A proper estimate of the azimuth cutoff is key to calculating the total wave energy accurately from the SAR inversion. In section 4, we present the wave attenuation results. Our discussion and conclusions follow in sections 5 and 6, respectively. This paper is followed by a Part 2 of Ardhuin et al. (2018) which includes numerical modeling of this event that provides further interpretation of the observed wave and ice patterns.

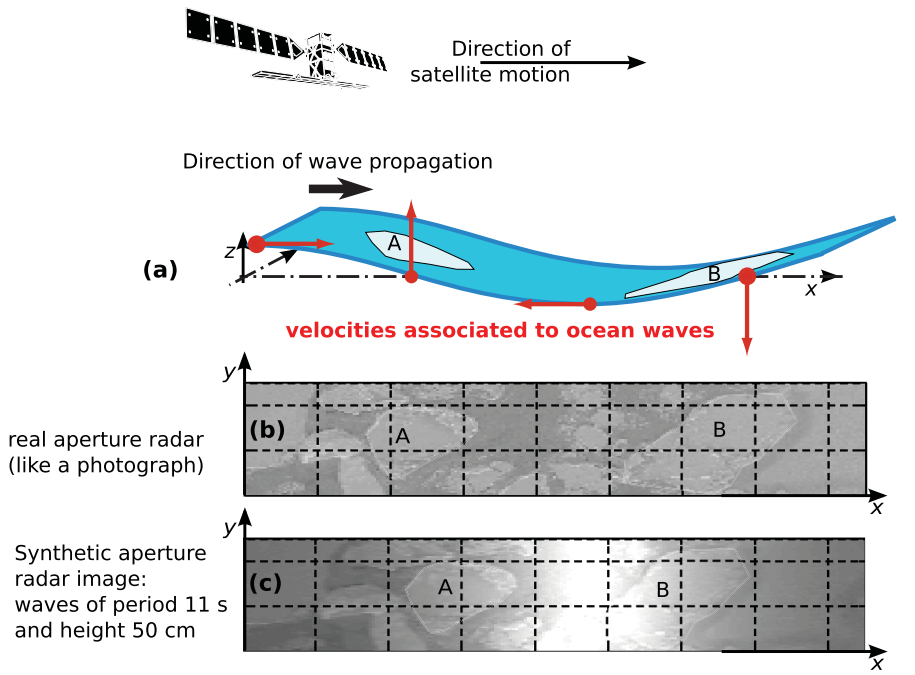

Figure 2. Principle of wave measurement by velocity bunching. (a) Schematic of radar flying over waves. (b) Hypothetical real aperture image with ice floes A and B smaller than the wavelength: the pixels in the real aperture image are at the true position of the targets. (c) Corresponding synthetic aperture radar image: the targets are displaced in the image as a function of their Doppler velocity. As a result, bright intensity lines appear in the regions of vertical velocity convergence (here the trough, but it would be the crest if waves propagate in opposite direction). This velocity bunching effect is constructive as long as the imaging parameter C_{AR} is less than 1 (see text).

2. Site Description, Methods, and Data Sets

2.1. Environmental Conditions

The field experiment took place aboard the R/V Sikuliaq from 1 October to 4 November 2015 (see Thomson et al., 2017, for an overview). The highest waves that were observed during the expedition occurred early on 12 October, with significant wave heights (H_s) up to 5.5 m. Deployment of a number of buoys captured the evolution of this event (termed Wave Experiment 3), which is described in detail by Rogers et al. (2016), Cheng et al. (2017), and Smith et al. (2018).

The sea ice conditions and sea state time history are summarized in Figure 3. This event has winds predominately from the East which is an ideal direction for wave growth since the largest open water fetch extends East-West during the Fall freeze (Stopa et al., 2016; Thomson et al., 2016). The maximum H_s during this event is above the 95th percentile based on a wave hindcast for this area covering the years 1992–2014 (Stopa et al., 2016).

Figure 3 shows the time series of the deployed in situ buoys during the event. Beginning on 11 October, the waves begins to steadily increase with the maximum H_s of 5.5 m recorded at 12 October 06:00 UTC. S1A passed later that day when significant wave heights were declining with values of at least 3 m in the ice-free ocean. The location of the ice edge, as defined by the 0.7 concentration contour from the Advanced Microwave Scanning Radiometer 2 (AMSR2), changed rapidly from 10 to 11 October (not shown), but was fairly stable on 12 October. The northernmost ice edge is located at 74.2°N (Figure 3a). At the time of the S1A image, most of the active buoys are located in a region with bands of pancakes in open water where the ice edge is not well defined. The ice thickness (Figure 3b), as estimated from ESA's soil moisture ocean salinity (SMOS) mission (Kaleschke et al., 2012), is approximately 10–30 cm for several hundred kilometers from the ice edge throughout the majority of the MIZ. Figure 3c shows the normalized variance from the S1A backscatter. The rougher sea ice clearly stands out (in blue), and the contour of 1.8 appears to be a good proxy for the ice edge in agreement with those indicated by the AMSR2 ice concentration and SMOS

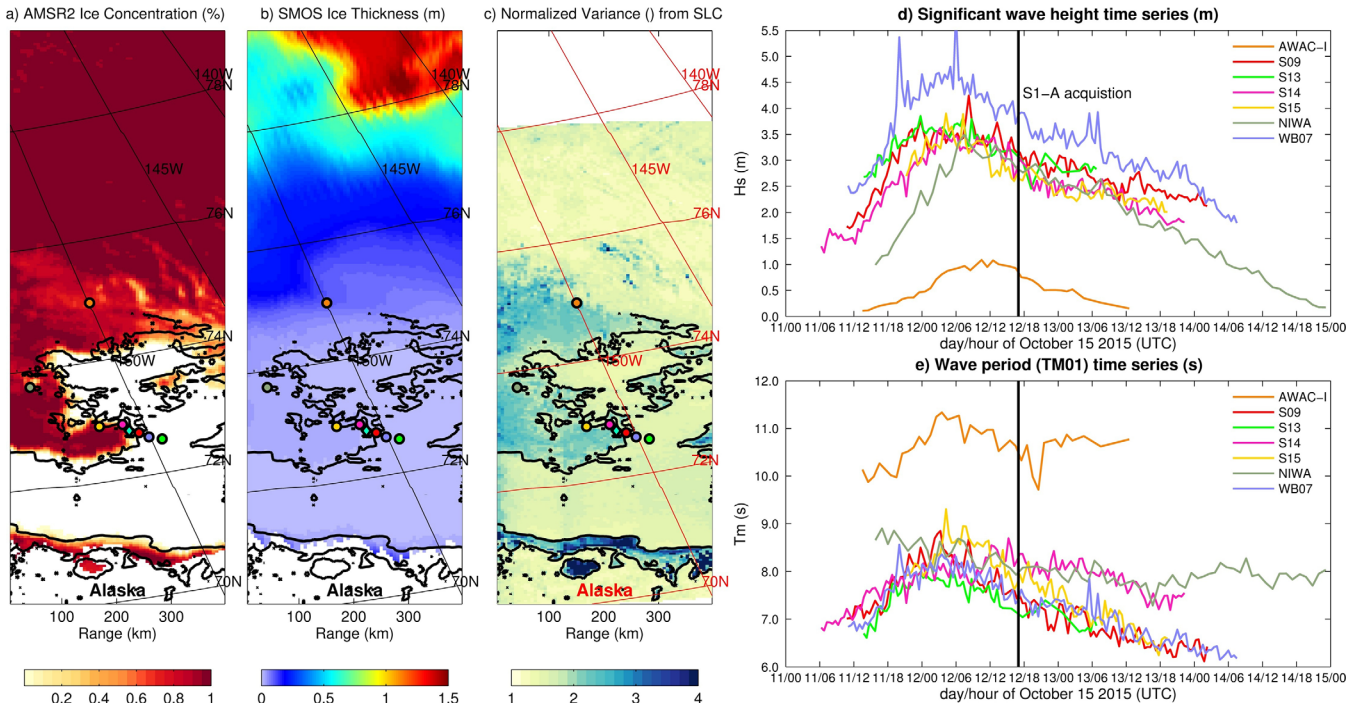

Figure 3. Ice conditions and the time history of the wave conditions close to the Sentinel-1A satellite pass. (a) The AMSR2 ice concentration, (b) the SMOS ice thickness in the Beaufort-Chuckchi Sea. (c) Normalized variance from SAR SLC data and the black contour of 1.8 is expected to represent the ice edge since it agrees with the other satellite products. The markers represent the locations of the in situ observations using the same color code as Figure 1. (d and e) The significant wave height and peak period time series from in situ observations for the storm event.

ice thickness. This contour is repeated in other maps for reference. In addition, the positions of in situ wave observations are shown using the same color code throughout the manuscript.

2.2. In Situ Wave Observations

During this storm event, in situ wave data were recorded from a Nortek AWAC under-ice (AWAC-I) acoustic Doppler profiler (ADCP) deployed on a mooring and three different types of wave buoys. Their locations corresponding to the S1A acquisition time are shown in Figures 3a–3c. The AWAC-I was deployed in 100 m water at 150°W,75°N, 100 km north from the ice edge. Surface wave spectra obtained from the moored AWAC-I are highly valuable because the location is positioned deep into the ice pack where the S1A wave estimations are most reliable. This instrument gives a H_s=0.95 m at the time of the S1A image, when the average H_s in closer to the ice edge is 3.0 m.

Wave spectra are also obtained from three different buoys. These include SWIFT buoys (Thomson, 2012) (denoted S09, S12, S13, S14, and S15), a "British wave buoy" WB07 (Doble & Wadhams, 2006), and a National Institute of Water and Atmospheric Research (NIWA) buoy (Kohout et al., 2014). Buoys all use an internal tri-axis inertial motion unit (IMU) at approximately the sea surface elevation to obtain true displacement time series used to calculate the wave spectra. Data were interpolated to the same frequency domain spanning 0.056–0.49 Hz prior to spectral analysis and computation of wave parameters. SWIFTs and the WBs both float at the sea surface in the water between floes, with a spar and pancake shape respectively, while the NIWA buoy sits on a sea ice floes (see cruise report for images Thomson, 2015), though the difference in shapes does not appear to significantly affect the observed response. All three buoys were cross checked during an earlier deployment during the field experiment in order to validate that they provided consistent wave spectra. However, Figure 3 shows that the H_s from WB07 is consistently higher than H_s from the nearby SWIFTs. We expect the H_s from WB07 might be anomalously high or the H_s from the SWIFTs might be biased low. The low-biased H_s from the SWIFTs could be related to an overly severe filter with reduces the measured wave energy. Positions are tracked using GPS. It was confirmed that all buoys in the region shown in Figure 1d have a horizontal motion that has the same amplitude as the vertical motion. This implies the in situ wave measurements are expected to be of good quality and the pancakes are rafted in

multiple layers with little resistance to converging and diverging motions. Darker bands in Figure 1d are expected to be pancake ice and the more oblique wave orientation is visible thanks to the longer cutoff wavelength, showing that the short unresolved waves are strongly attenuated in these bands.

The time series of measurements of wave height and period are given in Figures 3d and 3e. In situ wave spectra and derived parameters were computed with a 30 min average and use an upper wave frequency of 0.4 Hz to compute the wave parameters. Here we show (Figures 3d and 3e) the H_s and the average wave period (T_m)

$$H_s = 4\sqrt{\int_0^{0.4} E(f)df} \tag{1}$$

$$T_{m0,1} = 2\pi \frac{\int_0^{0.4} E(f)df}{\int_0^{0.4} (2\pi f)E(f)df} \tag{2}$$

where E is the wave spectrum and f is the wave frequency. The average wave period near the ice edge was 7.5–8.5 s. Deeper into the sea ice, at the AWAC-I, the dominant wave period is 10.5 s and calculated wavelength is 175 m (assuming linear wave dispersion without effects from sea-ice). The wave directions recorded at the ice edge, where SWIFTs and WB07 were located, are approximately from the ESE (120°–130°). In principle, wave direction could be estimated from the AWAC-I but the recorded acoustic Doppler signal is influenced by the ice motion, making the directional information unreliable. Here the SAR data can supplement the in situ observations by providing wave directions. The wave propagation direction at the AWAC-I is approximately from the South as observed by SAR and will be described later. The finite propagation time of the waves over these large distances makes the wavefield nonstationary and the interpretation of wave transformation is more complex. This issue is addressed in the discussion.

2.3. SAR Data and Processing

The Sentinel-1 SAR acquisition uses interferometric wide swath (IW) mode which gives a 400 km wide swath. S1A is a C-band radar and has a frequency of 5.4 GHz. This acquisition mode resolves waves and ice features with a spatial resolution of 10 m or less in the range direction (across the swath), and 14 m in azimuth (along the satellite track). The data products are freely available from the ESA Sentinel Data Hub. Incidence angles range from 30° to 46°. Both HH and HV polarization are available. We use HH polarization throughout this study.

We use two different level-1 (L1) products from the European Space Agency (ESA) (Sentinel-1, 2013). The first L1 product is the single look complex (SLC) which is georeferenced using orbit and data from the satellite. Each single look uses the full frequency bandwidth of the emitted signals and the phase information is conserved and saved as a complex number. The resolution in range and azimuth is approximately 4 and 14 m, respectively. The second L1 product is the ground range detected high resolution (GRDH) mode. This is focused SAR data that has been detected, multilooked and projected to ground range using an Earth ellipsoid model. The phase information is lost and the speckle noise is reduced at the cost of the geometric resolution. In GRDH, the resulting real-valued backscatter has spatial resolution of approximately 10 and 14 m. The GRDH product has its advantages because the entire satellite footprint is resolved. On the other hand, the SLC product is coherent over smaller along-track regions (with data gaps in between) corresponding to a focused burst of electromagnetic signals of approximately 2.75 s. The phase information of the SLC image is used to produce multiple looks which is particularly useful for reducing the speckle noise in wave measurements based on the cross spectra of different looks (Engen & Johnsen, 1995).

We apply the method of Ardhuin et al. (2017a) to estimate wave spectra throughout the GRDH image. There is only one wave system, so we skip directly to step two of the method. This event has a dominant wavelength of 175 m, corresponding to a narrow frequency spectrum. Therefore, we apply a high-pass spatial filter with a cutoff wavelength of 650 m on all subimages. We use subimages of 512 × 512 points which equates to 5.1×7.2 km with a 50% overlap of adjacent subimages. The nonlinearity of the image is quantified by the coefficient C_{AR}, originally defined by Alpers and Rufenach (1979) as:

$$C_{AR} = k_y UR/V \tag{3}$$

where k_y is the wave number in the azimuth direction, U is the amplitude of the wave orbital velocity along the line sight, $R = H/\cos(\theta_i)$ is the distance from the satellite to target, and θ_i is the incidence angle. For S1A, the altitude $H = 692$ km and satellite velocity $V = 7{,}450$ m s^{-1}. There is a unique solution of mapping the waveforms in the SAR imagery when $C_{AR} < 1$ (Ardhuin et al., 2017a). We refer to this as the "linear" SAR imaging regime. Following the quasi-linear theory of Hasselmann and Hasselmann (1991, equation (56)), the SAR image spectrum E_{ql} is reduced from the expected value E_l due to the azimuth cutoff effect. Using the usual definition of the azimuth cutoff λ_c given by Kerbaol et al. (1998), which is twice the value defined in Ardhuin et al. (2017a), we have

$$E_{ql}(k_x, k_y) = \exp\left[-k_y^2\left(\frac{\lambda_c}{\pi}\right)^2\right] E_l(k_x, k_y) \tag{4}$$

where k_x and k_y are the wave number in the range and azimuth, E_l is the linear approximation computed by mapping the displacement of each wave crest to orbital velocities. This quasi-linear approach is generally a good approximation of the full SAR transformation (see also Krogstad, 1992). It is thus essential to accurately estimate λ_c. This method can be applied to any SAR data that adequately resolves the orbital motion of waves in sea ice. The platform altitude and velocity will affect the clarity of the SAR images (e.g., R/V in equation (3)). For example, the X-band radar aboard TerraSAR-X described in Gebhardt et al. (2016) has a lower altitude than S1A and the correspondingly lower value of R/V gives a lower contrast in the SAR image.

Due to the dominant exponential factor in equation (4), a Gaussian function fit to the image spectrum in the azimuth direction in open water reasonably matches the satellite observations, giving a good estimate of λ_c (Kerbaol et al., 1998). Cross spectra from different "looks" during the SAR dwell time reduce the speckle noise and improves this estimation of λ_c. This is the main reason for our use of the L1 SLC product. Due to the projection of velocities on the line of sight, the cutoff wavelength as a function of the vertical root-mean-square velocity w_{rms} is minimum for waves propagating in the azimuth direction and maximum for waves in the range direction. The following equation from Lyzenga et al. (1985) relates λ_c to the variance of the wave orbital velocity

$$\frac{\pi H}{V} w_{\mathrm{rms}} \le \lambda_c \le \frac{\pi R}{V} w_{\mathrm{rms}} \tag{5}$$

The root-mean-square vertical velocity from the spectrum is given by

$$w_{\mathrm{rms}} = \left(\int_0^\infty (2\pi f)^2 E(f)\, df\right)^{1/2} \tag{6}$$

where f is the wave frequency, and $E(f)$ is the wave elevation power spectral density. This approximation works well when comparing data from Envisat and moored buoys and can be used to estimate the wave orbital velocity (Stopa et al., 2015).

3. Processing of SAR Images in the MIZ

The large spatial variation in the surface roughness makes estimation of geophysical parameters challenging. Indeed, as shown in Figure 2, the brightness patterns due to velocity bunching (an artifact of the synthetic aperture processing) are easy to associate with waves if (real aperture) radar backscatter varies at scales much smaller or much larger than the ocean wave wavelengths. When length scales of waves and ice features are on the same order of magnitude, separation of waves, and ice features fails and the wave heights are overestimated. Therefore, we first use a homogeneity test, described below, that helps flag subimages dominated by ice features. Next we present the important parameters related to the validity of SAR inversion including the azimuth cutoff, the minimum detectable wavelength observed by SAR. Finally, we present the wave parameters derived from the SAR spectra.

3.1. Spatial Homogeneity

The presence of both open water and ice within one Fourier Transform window can give particularly complex spectra that are not simply related to the wavefield. For example, the region in Figure 1d has large

variations of the radar normalized cross section (NRCS). Consistent with visual observations from R/V Sikuliaq and video taken from the SWIFT buoys, the darkest regions with low NRCS, are dominated by frazil and grease ice. The intermediate NRCS values with low azimuth cutoff (region-II: clearer wave patterns oriented toward the Northwest) corresponds to pancake ice, while the brighter regions with higher cutoff (region-I: more distorted wave patterns) correspond to open water. The change of wave directions across Figure 1d is a clear illustration of the distortion in the SAR processing: the cutoff effect. For example, the wave patterns in the SAR image over the region identified in the red ellipse (labeled "I") are orientated perpendicular to the range direction (East-West) while the region in the upper magenta ellipse (labeled "II") has waves crests orientated approximately 30° from the range (toward the Northwest direction). Where orbital velocities are largest, only the wave patterns in the range direction can be seen and the others are blurred.

We thus expect that region-I is nearly ice-free with a significant short wave component, whereas region-II is mostly ice-covered. An ice-free patch of ocean is shown in Figure 1e. Here wave patterns are observed and are mostly aligned perpendicular to the range direction and there is strong blurring throughout. Figure 1e is similar to the region-I of Figure 1d. Deeper into the sea ice, for $Y > 550$ km, the large variation in backscatter is caused by water openings (leads) which appear as dark bands between large ice floes, as shown in Figure 1b. The ice roughness also varies within the floes, possibly revealing the presence of previous leads that have refrozen and may appear brighter due to frost flowers (Kaleschke & Heygster, 2004). In order to separate between ice features and ocean wave signatures, we implement the homogeneity test of Koch (2004) on the GRDH L1 data.

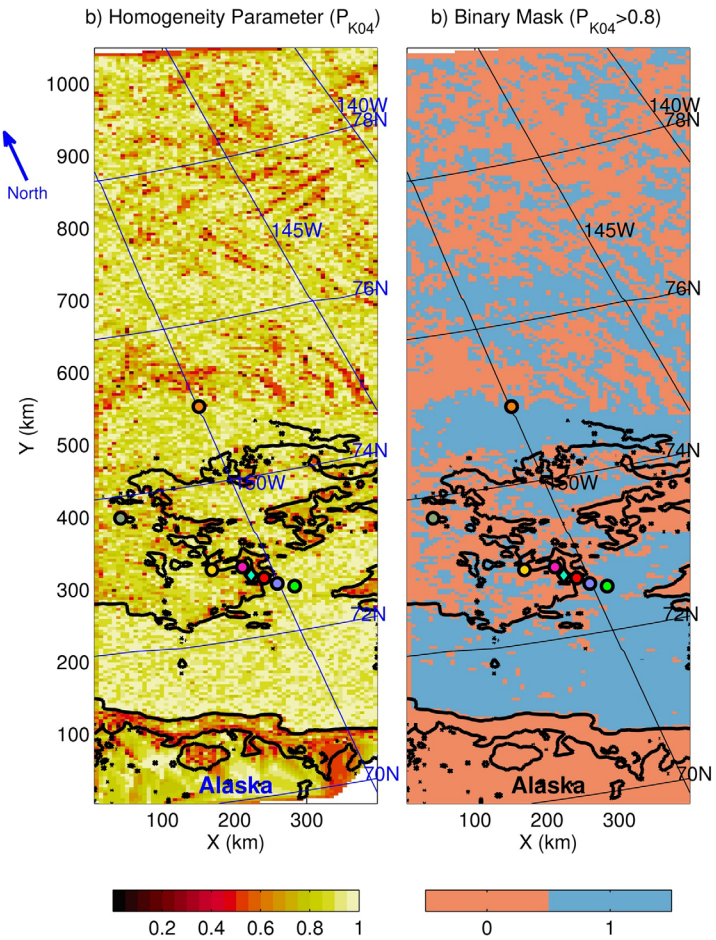

Figure 4. Homogeneity of S1-A SAR image where (a) the homogeneity parameter, P_{K04} of Koch (2004), computed at 160 m and downscaled to grid spacing of SAR GRDH processing (approximately 5–7 km) and (b) a binary map of P_{K04} (i.e., when $P_{K04} > 0.8$, the sub-image is considered homogeneous and remapped to one). The markers represent the locations of the in situ observations using the same color code as Figure 1 and the black contour represents the SAR ice edge.

The homogeneity parameter of Koch (2004) (their equation (22) which we refer to as P_{K04}) plotted in Figure 4 is the root mean square of four different parameters that capture various features of the images. The calculation of P_{04} is performed at a very high resolution (160 m) compared to our GRDH subimages of 5.1×7.2 km. These 160 m grid cells are remapped to our subimage GRDH resolution by linear interpolation. Our purpose is to identify the small scale ice features that might affect the SAR inversion. If P_{K04} is closer to one the region is expected to be homogeneous. Figure 4a shows the noisy nature of SAR backscatter which contains ice features, ocean waves (in and out of sea ice), and ice-free ocean (could contain atmospheric effects). We notice a distinct change in P_{K04} (Figure 4a) approximately near $Y = 550$ km which represents a change in sea ice properties. Even in the ice-free ocean ($150 < Y < 250$ km) some variability exists on small scales and might be related to wave or atmospheric effects. After the down-sampling to the GRDH subimage resolution, we use a threshold of 0.8 to define homogeneous subimages as shown in Figure 4b.

3.2. SAR Inversion Parameters and Orbital Wave Velocity

Based on equation (4), the azimuth cutoff wavelength λ_c is an important parameter that must be estimated from the SAR image. Over the open ocean, fitting a Gaussian function to the autocorrelation in the azimuth direction is a reasonable method to estimate λ_c (Kerbaol et al., 1998; Stopa et al., 2015). In mixed water-ice conditions it is unclear how the method will perform; therefore we take opportunity to compare the in situ observations to the SAR estimates.

Following Chapron et al. (2001), we form three different "looks" from the L1 SLC data, that can be interpreted as images acquired at different times with a time separation of 0.2 s. We compute the cross spectra between looks 1 and 2 and looks 2 and 3 and then average these two cross spectra. This reduces the contribution of speckle noise thanks to its fast decorrelation time (Engen & Johnsen, 1995). The resulting spectra have lower energy levels at the

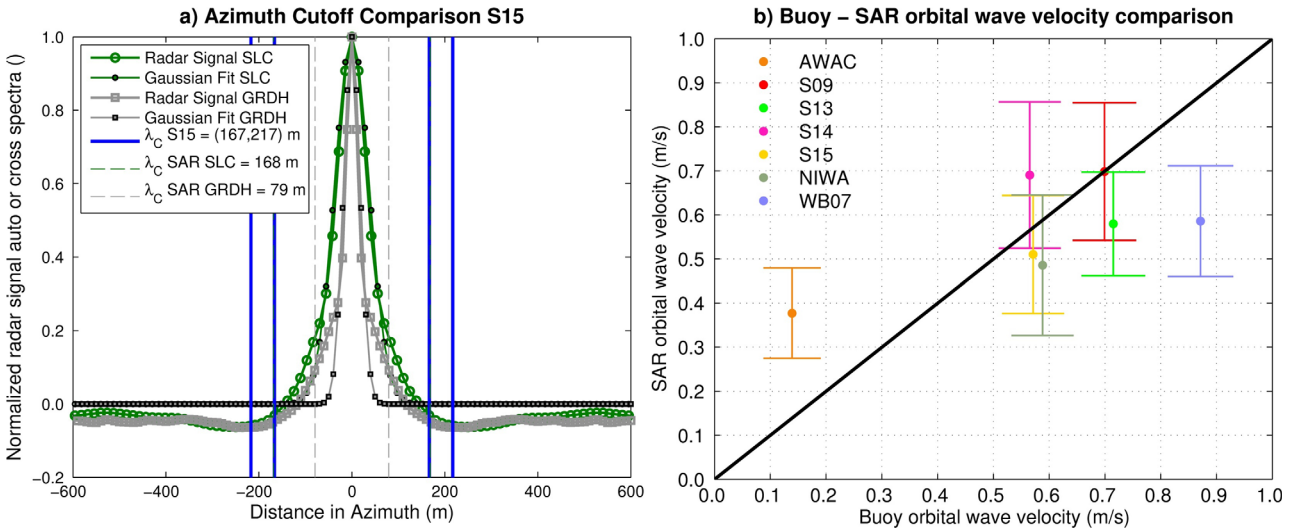

Figure 5. (a) An example Gaussian fit to the radar signal and the estimated azimuth cutoff (λ_C) at SWIFT 15. The green line with green circles is the radar signal from the SLC cross spectra and the green line with small black circles is the Gaussian fit. The gray line with gray squares is the radar signal from the GRDH auto-spectra and the gray line with small black square is the Gaussian fit. The solid blue vertical lines denote the expected range of azimuth cutoff from the buoy (see equation (5)). The dashed green and gray lines are the SAR SLC and GRDH λ_c, respectively. (b) A comparison of wave orbital velocity in mixed ocean-ice conditions for all seven in situ observations. The *x* axis represent the buoy observations and the *y* axis is the SAR estimates where the color denotes the buoy. The error bars represent the range of expected λ_c based on equation (5).

lowest frequencies, compared to spectra estimated from the amplitude image, leading to a more accurate estimation of the cutoff wavelength λ_c. One example is given in Figure 5a. The cross-correlation function of SLC-looks is shown in green while the gray line represents the autocorrelation of the GRDH image. The speckle produces a sharper peak at zero-lag, and the standard deviation of the Gaussian fit is much smaller resulting in a lower λ_c of 79 m compared to the SLC λ_c of 170 m. Note that radar SLC signal (green line with green circles) and Gaussian fit (green line with small black circles) are nearly identical and the lines are over-plotted on each other. The range of expected λ_c from S15 is given by the vertical blue lines (equation (5)). Note that the SAR SLC λ_c (light dashed green) overlays on the lower limit of the buoy.

The azimuth cutoff is transformed into a vertical root-mean-square orbital velocity using equation (6) and compared to the in situ observations in Figure 5b. The orbital velocities from the buoys are computed using an upper cutoff frequency of 0.4 Hz, which only reduces the buoy velocity variance by a few percent. From these seven data points, it is difficult to generalize the ability of the S1A SAR in IW mode to estimate the orbital wave velocity in mixed ocean-ice conditions. However the expected range, denoted by the vertical error bar, of SAR orbital motions (e.g., equation (5)) typically intersect the bisector. The comparisons with the SWIFTs are within 0.1 m s^{-1} or approximately λ_c=50 m. The exception is at the AWAC-I located further into the sea ice where the $\lambda_{c\ SAR}$=125 m while the buoy $\lambda_{c\ AWAC-I}$=60 m. The overestimation at the AWAC-I could be caused by ice features associated to floes with diameters comparable to the dominant wavelength. A possible evidence of the presence of such floes is the complex texture of the SAR image around the AWAC-I (Figure 1c). The other exception is at WB07 which typically has higher wave energy than the SWIFTs (see Figures 3d and 3e).

When applying the SAR inversion method of Ardhuin et al. (2017a), waves in ice must be properly imaged by the radar. There are three important criteria:

1. The wavelength must be larger than the azimuth cutoff ($L_p > \lambda_c$).
2. The waves should approximately be within the linear SAR imaging regime ($C_{AR} < 1$).
3. The pattern of radar backscatter should be dominated by the velocity bunching effect.

In Figure 6, we show both parameters related to the first two criteria. Of course the azimuth cutoff is largest in the ice-free regions and is mostly larger than 200 m. Once ice is present, the high frequency waves are dissipated and λ_c reduces 50 m across 2–4 subimages (10−40 km). For example, in the fuzzy region

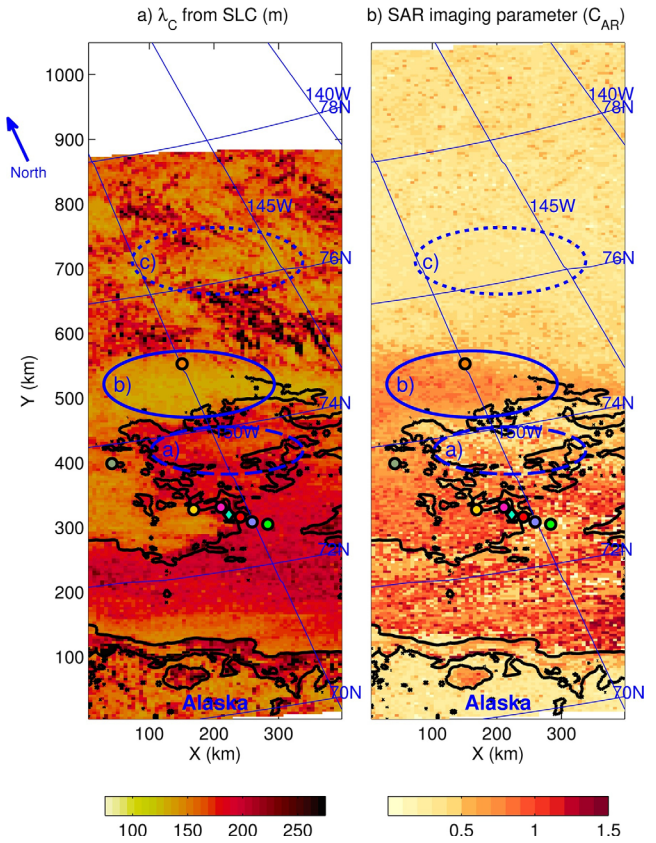

Figure 6. Geophysical parameters important for the SAR inversion: (a) The azimuth cutoff λ_c computed from the SLC image and (b) the SAR imaging coefficient of Alpers and Rufenach (1979) (C_{AR}). Refer to the main text for a description of the highlighted regions: a, b, and c.

(composed of ice and open water) where the buoys are located, λ_c changes by 50–100 m within 20–30 km. Beyond this sharp decay and ignoring the scatter from the ice, λ_c remains relatively flat around the values of 100–125 m for Y >475. We expect λ_c=125 m is too large to solely represent the geophysical nature of the waves as the short waves continue to dissipate. So perhaps the SAR-derived azimuthal cutoff in the ice is only valid close to the ice edge. The quality (clarity) and resolution of the image could also affect the estimate of λ_c. This is where a platform of lower altitude like TerraSAR-X could be very useful.

In Figure 6b, we show C_{AR} defined from the root-mean-square velocity, which quantifies the feasibility of applying a deterministic SAR inversion. Typically in the ice-free ocean C_{AR} is larger than 1 but it varies considerably in the region with $Y \in [150, 250]$ km, possibly due to the contribution of ice features that are misinterpreted as orbital velocities. Further into the sea ice for $550 < Y < 750$ km, C_{AR} is always less than 1. For $Y > 750$, the spatial variability of C_{AR} is expected to be related solely to ice features perpendicular to the azimuth direction and the contribution from waves is minimal.

We identify three distinct regions to describe the feasibility of applying the SAR inversion. Region *a* is relatively homogeneous (see also P_{K04} in Figure 4) and $C_{AR} < 1$. However, $\lambda_c > 200$ m suggests some high frequency waves are present and we expect this region is mostly ice-free. So in region *a*, we cannot apply the SAR inversion. In region *b*, λ_c is typically 110–140 m, $C_{AR} < 1$, and it is homogeneous. Therefore, this region is optimal to perform the SAR inversion. Deeper into the ice pack, we observed that the ice features are causing the variability in the SAR backscatter. For example, ice leads as in Figure 1b and possibly multiyear floes contribute to the backscatter variability. In region *c*, we can see that the azimuth cutoff is affected by the ice features and possibly the image noise, but $C_{AR} < 0.5$ so the waves are well resolved by the inversion. So region *c* will have to be well-flagged using the filtering techniques described above.

3.3. Wave Parameters

Using all of the information, we are able to calculate the significant wave height (H_s) from the SAR data from properly flagged subimages, using the following criteria:

1. $P_{K04} > 0.8$ to ensure the grid cell has homogeneous backscatter (i.e., moderate ice features).
2. Further into the sea ice, for $Y > 600$ km we take a stricter constraint $P_{K04} > 0.95$ to help remove the presence of ice features which are prevalent here. Additionally we restrict $C_{AR} < 0.3$ to remove subimages corrupted by ice features directed along the azimuth direction.
3. $\lambda_C < 150$ m to ensure the dominant wavelength of approximately 175 m is resolved.
4. $C_{AR} < 1$ to ensure the waveforms are properly imaged by the SAR.

In Figure 7a, we show H_s from subimages that passed our criteria. The H_s is computed from the SAR wave spectra and includes the λ_C correction (equation (4)). In spite of a sparse coverage caused by these criteria, the spatial coverage is impressive and waves are measured over 500 km from the first valid acquisitions near $Y = 300$ km to the last near $Y = 800$ km. In total, there are 2,360 spectra from independent subimages that satisfy these criteria.

The other striking feature is the spatial variability. For example at $Y = 500$ km, the wave heights are larger at $X = 50$ km compared to $X = 350$ km. This is due to the fact that the waves dissipate less as they propagate through the ice-free region in the center of the image. The dominant direction is from the ESE. Within the ice peninsula ($X = 100$–200 km and $Y = 300$–400 km) wave heights range from 2.5 to 3.5 m and a few points

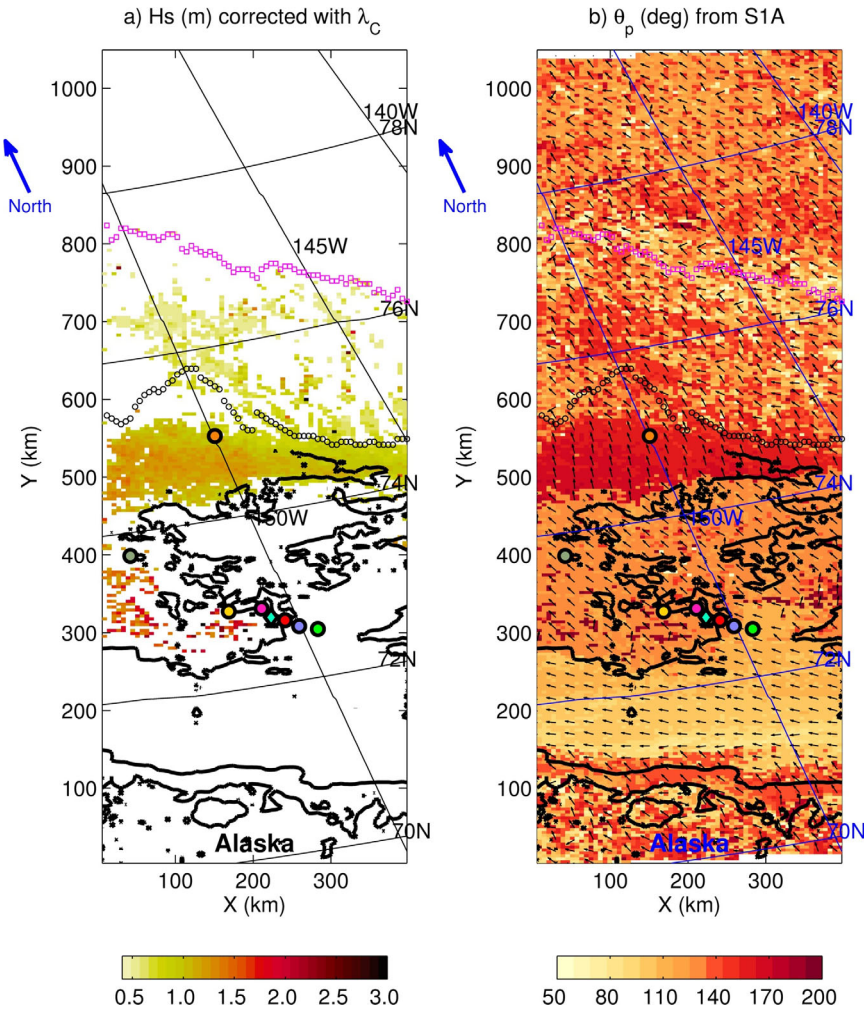

Figure 7. Wave parameters from computed from the SAR spectra: (a) The significant wave height of the "best" quality data and (b) shows the peak SAR wave direction (using meteorologic convention). The black circles represent the first azimuth for each range position where the presence of an ice lead was detected. The magenta squares represent the upper limit of largest azimuth position where waves were visually observed.

exceed 4 m agreeing with the H_s in situ observations ($H_s \in [2.6, 3.4]$ m). The H_s at the AWAC-I without the λ_c correction is 0.86 cm. The SLC SAR λ_c is 125 m giving a corrected H_s of 0.97 m closely matching the AWAC-I measured H_s of 0.95 m. Deeper into the ice, the λ_c could be introducing errors to the H_s because λ_c was overestimated at the AWAC-I and did not decay with distance into the ice as we expect the short waves to continually dissipate. Notice that region *b* identified in Figure 6 is well resolved by the SAR and the majority of the observations are located here. Further into the sea ice ($Y > 600$ km), the observations are more sparse since the ice features distort the SAR inversion. Notice several anomalously large wave heights are observed relative to the majority of the other observations in this region. We attempted to remove the anomalously large H_s here by implementing condition 2 above. It remains difficult to separate the ice features and ocean waves.

We show the peak wave direction from the SAR wave spectra ("propagating from" i.e., 180° = from South to North) in Figure 7b. The ice-free region clearly stands out with directions from ESE to E which is mainly due to the azimuth cutoff effect. Once ice is present the wave direction dramatically changes 20–30° in the clockwise direction. Deeper into the ice (region b of Figure 6), the waves are nearly directed to the North with an average of direction of 355°. In addition to the ice edge, there is another change of 20° in the clockwise direction along $Y = 475$ km. We expect the more dramatic changes in directions are effects of refraction (at the ice edge or due to a change in the ice thickness) (e.g., Shen et al., 2018). The overall pattern of

the wave directions can be explained by the angular spreading of wave energy and can be captured by a numerical wave model without including such a refraction (see Part 2: Figure 9a, Ardhuin et al., 2018). Deeper into the ice $Y > 600$ km the ice features distort the wave directions but in general the quality subimages have wave directions propagating to the North (355°).

Figure 7 also shows an estimate of large-scale ice features (leads and floes) detections. For each X position, the black circle marks the Southernmost Y position where large-scale ice features were detected. This detection is done by first computing a one-dimensional spectrum from the GRDH product to produce an image modulation spectrum. The spectrum is then normalized by the maximum energy contained in wavelengths from 100 to 300 m (the wavelength range of the dominant sea state). We found that when the energy exceeds a threshold of 0.8 for wave numbers larger than 1 km, ice features are not generally present. This line physically represents a distinct change in the sea ice conditions which we expect is indicative of the interaction between the waves and sea ice.

The magenta squares represent the Northern limit of waves visually observed in the subimages. North of this line, wave features are hard to detect. Proper definition of this upper extent has practical applications such as understanding the influence of waves on the sea ice. So the region from the ice edge to the magenta line can be considered the wave-MIZ. Beyond the magenta line waves might be present, with $H_s < 0.3$ m, however the Sentinel-1A SAR instrument is not precise enough to resolve their orbital motions given the background variability in backscatter and instrument noise in IW mode.

4. Wave Attenuation

The observed wave conditions are complex, with a diffuse ice edge around the buoys and a complicated fetch geometry. The waves have a veering direction as a result from ESE in the ice-free region to a North direction within the sea ice. To analyze the wave attenuation, we take six different transects along the dominant wave heading of due North. Starting from $Y = 475$ km we bin the observations into 50 km sections in the X direction (see Figure 8a and denoted T1 = track 1, etc.).

We show the average wave period and six individual tracks across the MIZ in Figure 8. The wave period ranges from 10 to 12.5 s. Beyond this range the values are influenced by the ice features. Notice the wave period is larger on the left side of the image similar to the H_s map. Otherwise there is subtle indication that the wave period increases further into the sea ice.

We plot the wave variance ($E = (H_s/4)^2$) as a function of distance in Figures 8b–8g. The vertical dashed and solid blue lines designate the first and last ice lead locations as defined in Figure 8a. We show the wave variance versus distance on a linear-logarithm plot to explore the feasibility of an exponential decay

$$E_i = E_0 \exp(\alpha x) \tag{7}$$

where E_0 is the initial wave energy observation, and E_i are the SAR observations along the tracks, i is the index, x is the distance in meters, and α is the attenuation coefficient. In track-1, all observations are before the ice leads and the exponential attenuation rate is -1.6×10^{-5} m^{-1}. For track-2, we see that a single exponential function matches the observations but with a large data gap from 50 to 150 km. For tracks 3 and 4, there are a sufficient number of data both before and after the ice leads. In these two transects, it is difficult to fit an exponential function with a single attenuation rate. This suggests there are two different attenuation rates that differ by an order of magnitude before and after the ice leads. Within the first 50–100 km the attenuation rate is -1.4 to -1.1×10^{-5} m^{-1} while after the lead the attenuation is much weaker at -2.9 to -1.9×10^{-6} m^{-1}. Tracks 5 and 6 also show the wave decay changes before and after the leads but this effect is more subtle. Notice in all tracks the SAR observations are more variable deep into the sea ice. The outliers (denoted by blue circles) were not included in the computation of the decay rates. In short, we find evidence that waves attenuate differently before and after the presence of ice leads as denoted by the black line in Figures 7 and 8. Before the leads waves dissipate at higher rates compared to deeper into the sea ice.

Along each of these tracks the wave period increases with distance. Since short waves attenuate faster than longer wavelengths, it is expected that deeper in the MIZ, longer wavelengths are present. However, the storm frequency dispersion could also cause this pattern. This issue of stationary is discussed more thoroughly in the following section.

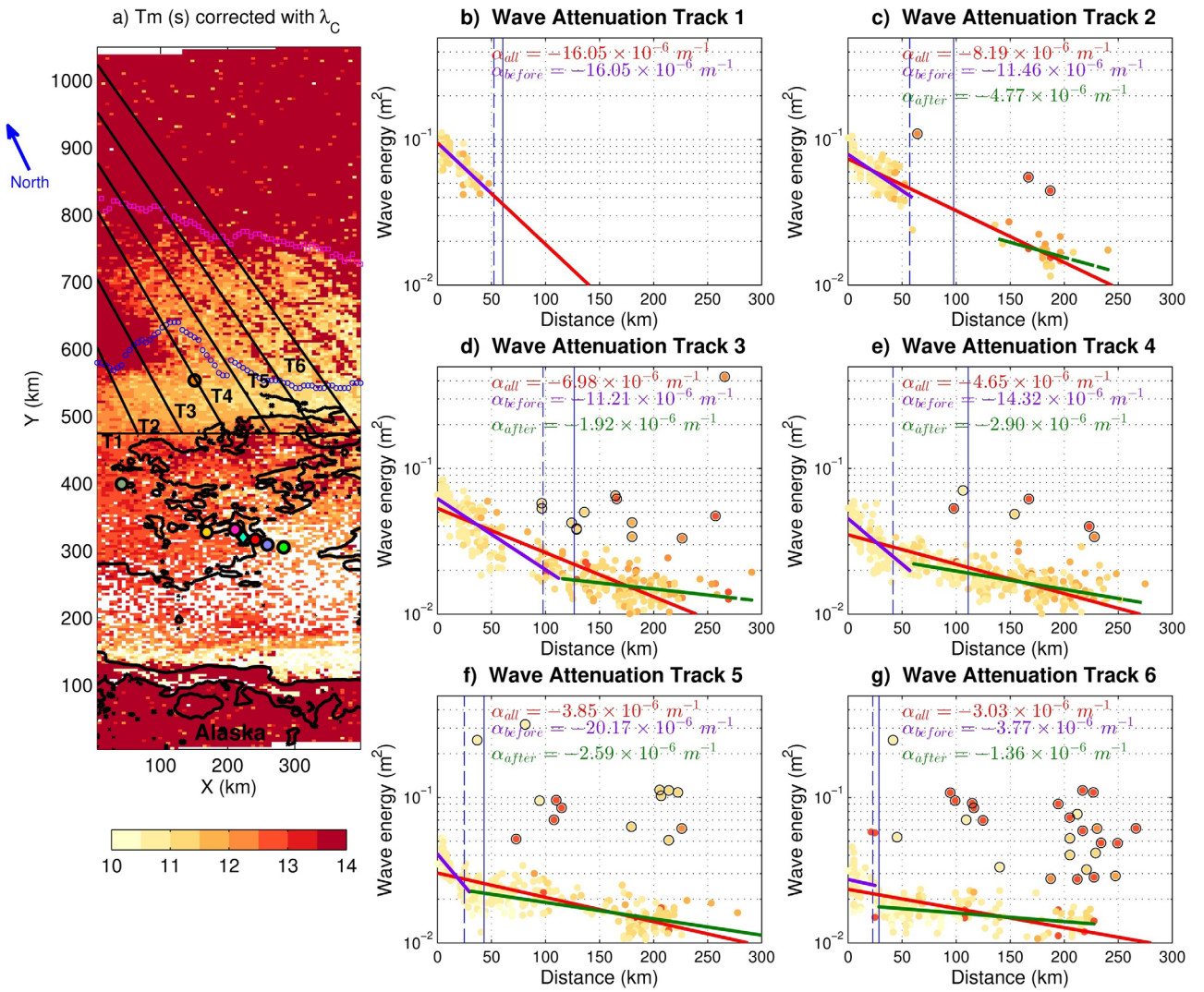

Figure 8. Wave decay: (a) the average wave period from SAR the dominant wave direction of waves propagating North (355°) in six distinct tracks identified in black. (b–g) the wave attenuation plotted as function of distance relative to $Y = 475$ km with a linear-log scaling. The red line is a linear fit of the wave energy for the entire track, the purple line is a linear fit of the wave energy before the change in ice features, and the green line is a linear fit of the wave energy after the change in ice features. The outliers are denoted by blue circles and are not included in the calculation of the attenuation rates. The change in ice features is designated by the vertical black lines: dashed/solid represent the first/last instance of ice leads and correspond to the blue circles in Figure 8a. The colors in Figures 8b–8g denote the average wave period with the same color scale in Figure 8a.

5. Discussion

The assumption of the wave stationarity might be invalid over these large-scales because the same wave packet takes a considerable amount of time to propagate a few hundred kilometers across the MIZ. In particular, waves with a period of 10.5 s have a group speed of 8.2 m s^{-1}; hence, the wave energy travels 400 km in 13.5 h. Given the decreasing trend in wave height shown in Figure 3d, the spatial attenuation that we observe should be larger than the attenuation that would be observed in stationary conditions. We do not observe larger waves deep into the ice pack so we expect that the sea ice conditions are controlling the observed wave decay and not dispersion. Using a numerical model in Part 2, we will compare various attenuation parameterizations to these observations, taking into account the complex fetch geometry and non-stationarity of the wavefield (Ardhuin et al., 2018).

While we made serious efforts to separate sea ice features from wave features, there are probably remaining ice features that contaminate the wave spectra. This is especially true far into the ice pack where leads and waves are easily observed (e.g., Figure 1b). The spatial homogeneity test of Koch (2004) was developed for

a wide range of conditions but other spatial gradient calculations could be implemented to best test for homogeneity of the sea ice features. Having an optimal way to separate ice and wave features remains challenging and is a major hurdle in automating such a system to estimate wave spectra in sea ice with proper flagging. At intermediate locations, near the AWAC-I, the possible presence of ice features at scales similar to the wavelength poses a real challenge.

In this study, we are able to estimate wave heights across several hundred kilometers of MIZ. The SAR observations show the spatial variability of the wave and sea ice features at scales ranging from 100 m to 1,000 km. The kilometer-scale resolution can supplement the data gap by providing a broader spatial view especially compared to previous studies from experiments over short distances (Wadhams et al., 1988) or studies that calculate wave attenuation using two locations (Kohout et al., 2014).

The SAR observations reveal a unique wave attenuation pattern characterized by a strong decay into a moderate/weak decay. The observed exponential decay complements many others (Kohout et al., 2014; Liu et al., 1992; Wadhams et al., 1988). However, using a single exponential decay to describe wave attenuation over 300 km is difficult in several of our tracks (Figure 8). We expect this is due to the change in sea ice conditions and this has implications on the wave-ice mechanics. The piecewise exponential attenuation has strong decay of approximately $\alpha = -1.5 \times 10^{-5}$ m^{-1} and the moderate/weak decay of $\alpha = -2.4 \times 10^{-6}$ m^{-1} before and after the noted change in sea ice conditions. Our interpretation is that for locations 50–100 km before the ice leads (black line in Figure 7), and beyond, the young sea ice is composed of large floes ($>1/2 \times Lp$). For locations closer to the ice edge, the sea ice is most likely broken up by the waves.

The ice state and the waves are probably connected: broken ice may be less effective in dissipating wave energy (e.g., Collins et al., 2015), than if wave energy is dissipated by ice flexure. In contrast, if wave attenuation is dominated by scattering, broken ice may enhance the wave attenuation. However, the presence of long wave crests in the SAR image suggests that scattering should have a minimal impact for the dominant 10 s waves. Also, dissipation due to ice flexure may be nonlinear with a stronger decay for larger wave heights (Cole & Durell, 2001).

In the rapid decay region ($500 < Y < 575$ km), the sea ice reduces the wave heights to a certain threshold where the sea ice no longer breaks. The sea ice is expected to largely be first year ice. Once leads are present we expect that the young first year ice has grown thicker and become more consolidated into floes. The difficulty is that there may still be large floes where we see no leads, and the backscatter of the image shows some differences between $450 < Y < 500$ km. These questions will be taken up again in Part 2 (Ardhuin et al., 2018).

6. Conclusion

Ice features introduce variations of the Normalized Radar Cross Section (NRCS) that contribute to the patterns in SAR imagery, making it difficult to estimate wave spectra from SAR imagery over sea ice using the method of Ardhuin et al. (2017a). Here we developed and implemented specific flagging and cutoff correction algorithms that were validated using in situ data. To our knowledge, this is the first large-scale and semiautomatic application of a wave height measurement method from SAR imagery in sea ice. This gives a unique view of wave evolution covering 400 km of the MIZ at 5 km resolution. We find a unique pattern of wave attenuation characterized by a piecewise exponential decays. This transition coincides with an observed change in the SAR backscatter which is indicative of a change in the young sea ice conditions (e.g., floe size, thickness, etc.). This supports the idea of having multiple wave decay mechanisms within a wave model. The resulting wave heights reveal an attenuation that is spatially variable. This application of wave retrieval across a wide swath image clearly shows the potential of this new type of data for investigating wave-ice interactions.

Given the rapidly shrinking Arctic sea ice (Khon et al., 2014), waves should play a larger role in the Arctic Ocean, possibly contributing to a wider MIZ. It is thus critical to measure waves and sea ice properties, both of which can be achieved by ESA's Sentinel-1 constellation. The occasional acquisition of IW mode data, in combination with the usual Extended Wide Swath (EW) mode, could be programmed during storm or swell events, as now done for hurricanes over the global ocean. This would enhance the science of wave-ice interactions. As a complement, dedicated satellite missions that would measure waves in and around the ice, such as the proposed Sea Surface Kinematics Multiscale Monitoring mission (SKIM, Ardhuin et al., 2018), can provide routine measurements of waves that are needed for operational applications.

Acknowledgments
We would like to thank the two reviewers for their comments that have improved this paper. This work was supported by EU-FP7 project SWARP under grant 607476, ONR grant N0001416WX01117, and CNES. It is based on observations with Sentinel 1 kindly provided by ESA. Support from LabexMer via grant ANR-10-LABX-19-01 is gratefully acknowledged. The northern AWAC was deployed and recovered by the NSF-funded BGOS (Beaufort Gyre Observing System) program. Data, supplemental material, and a cruise report can be obtained: http://www.apl.uw.edu/arcticseastate. AMSR2 sea ice concentrations can be obtained: http://doi.org/10.5067/AMSR2/A2_SI12_NRT. SMOS sea ice thickness product can be obtained: https://icdc.cen.uni-hamburg.de/1/daten/cryosphere/l3c-smos-sit.html.

References

Alpers, W., & Rufenach, C. (1979). The effect of orbital motions on synthetic aperture radar imagery of ocean waves. *IEEE Transactions on Antennas and Propagation*, *27*(5), 685–690. https://doi.org/10.1109/tap.1979.1142163

Ardhuin, F., Aksenov, Y., Benetazzo, A., Bertino, L., Brandt, P., Caubet, E., et al. (2017b). Measuring currents, ice drift, and waves from space: The Sea Surface KInematics Multiscale monitoring (SKIM) concept. *Ocean Science Discussions*. https://doi.org/10.5194/os-2017-65

Ardhuin, F., Boutin, G., Stopa, J. E., Girard-Ardhuin, C. M., Thomson, F., Kohout, J., et al. (2018). Wave attenuation through an arctic marginal ice zone on October 12, 2015. Part 2: Numerical modeling of waves and associated ice break-up. *Journal of Geophysical Research: Oceans*, *123*, https://doi.org/10.1002/2018JC013784

Ardhuin, F., Chapron, B., Collard, F., Smith, M., Stopa, J. E., Thompson, J., et al. (2017a). Measuring ocean waves in sea ice using SAR imagery: A quasi-deterministic approach evaluated with sentinel-1 and in-situ data. *Remote Sensing of Environment*, *189*, 211–222.

Ardhuin, F., Collard, F., Chapron, B., Girard-Ardhuin, F., Guitton, G., Mouche, A., et al. (2015). Estimates of ocean wave heights and attenuation in sea ice using the SAR wave mode on sentinel-1A. *Geophysical Research Letters*, *42*, 2317–2325. https://doi.org/10.1002/2014GL062940

Ardhuin, F., Sutherland, P., Doble, M., & Wadhams, P. (2016). Ocean waves across the arctic: Attenuation due to dissipation dominates over scattering for periods longer than 19 s. *Geophysical Research Letters*, *42*, 2317–2325. https://doi.org/10.1002/2016GL068204

Chapron, B., Johnsen, H., & Garello, R. (2001). Wave and wind retrieval from SAR images of the ocean. *Annals of Telecommunications*, *56*, 682–699.

Cheng, S., Rogers, W. E., Thomson, J., Smith, M., Doble, M. J., Wadhams, P., et al. (2017). Calibrating a viscoelastic sea ice model for wave propagation in the arctic fall marginal ice zone. *Journal of Geophysical Research*, *122*, 8770–8793. https://doi.org/10.1002/2017JC013275

Cole, D. M., & Durell, G. D. (2001). A dislocation-based analysis of strain history effects in ice. *Philosophical Magazine A*, *81*(7), 1849–1872. https://doi.org/10.1080/01418610108216640

Collins, C. O. III, Rogers, W. E., Marchenko, A., & Babanin, A. V. (2015). In situ measurements of an energetic wave event in the Arctic marginal ice zone. *Geophysical Research Letters*, *42*, 1863–1870. https://doi.org/10.1002/2015GL063063

Doble, M. J., & Wadhams, P. (2006). Dynamical contrasts between pancake and pack ice, investigated with a drifting buoy array. *Journal of Geophysical Research*, *111*, C11S24. https://doi.org/10.1029/2005JC003320

Engen, G., & Johnsen, H. (1995). SAR-ocean wave inversion using image cross spectra. *IEEE Transactions on Geoscience and Remote Sensing*, *33*(4), 1047–1056. https://doi.org/10.1109/36.406690

Gebhardt, C., Bidlot, J.-R., Gemmrich, J., Lehner, S., Pleskachevsky, A., & Rosenthal, W. (2016). Wave observation in the marginal ice zone with the TerraSAR-x satellite. *Ocean Dynamics*, *66*(6–7), 839–852. https://doi.org/10.1007/s10236-016-0957-8

Hasselmann, K., & Hasselmann, S. (1991). On the nonlinear mapping of an ocean wave spectrum into a synthetic aperture radar image spectrum and its inversion. *Journal of Geophysical Research*, *96*(C6), 10,713–10–729.

Kaleschke, L., & Heygster, G. (2004). Toward multi-sensor microwave remote sensing of frost flowers on sea ice. *Annales Geophysicae*, *39*, 219–222. https://doi.org/10.3189/172756404781814267

Kaleschke, L., Tian-Kunze, X., Maaß, N., Mkynen, M., & Drusch, M. (2012). Sea ice thickness retrieval from SMOS brightness temperatures during the arctic freeze-up period. *Geophysical Research Letters*, *39*, L05501. https://doi.org/10.1029/2012GL050916

Kerbaol, V., Chapron, B., & Vachon, P. W. (1998). Analysis of ERS-1/2 synthetic aperture radar wave mode imagettes. *Journal of Geophysical Research: Oceans*, *103*(C4), 7833–7846. https://doi.org/10.1029/97JC01579

Khon, V. C., Mokhov, I. I., Pogarskiy, F. A., Babanin, A., Dethloff, K., Rinke, A., et al. (2014). Wave heights in the 21st century Arctic ocean simulated with a regional climate model. *Geophysical Research Letters*, *41*, 2956–2961. https://doi.org/10.1002/2014GL059847

Koch, W. (2004). Directional analysis of SAR images aiming at wind direction. *IEEE Transactions on Geoscience and Remote Sensing*, *42*(4), 702–710. https://doi.org/10.1109/tgrs.2003.818811

Kohout, A. L., Williams, M. J. M., Dean, S. M., & Meylan, M. H. (2014). Storm-induced sea-ice breakup and the implications for ice extent. *Nature*, *509*(7502), 604–607. https://doi.org/10.1038/nature13262

Krogstad, H. E. (1992). A simple derivation of Hasselmann's nonlinear ocean-synthetic aperture radar transform. *Journal of Geophysical Research*, *97*(C2), 2421–2425.

Liu, A. K., & Mollo-Christensen, E. (1988). Wave propagation in a solid ice pack. *Journal of Physical Oceanography*, *18*(11), 1702–1712. https://doi.org/10.1175/1520-0485(1988)018<1702:WPIASI>2.0.CO;2

Liu, A. K., Vachon, P. W., Peng, C. Y., & Bhogal, A. (1992). Wave attenuation in the marginal ice zone during LIMEX. *Atmosphere-Ocean*, *30*(2), 192–206. https://doi.org/10.1080/07055900.1992.9649437

Lyzenga, D. R., Shuchman, R. A., Lyden, J. D., & Rufenach, C. L. (1985). SAR imaging of waves in water and ice: Evidence for velocity bunching. *Journal of Geophysical Research*, *90*(C1), 1031–1036. https://doi.org/10.1029/jc090ic01p01031

Marshall, D. P., & Zanna, L. (2014). A conceptual model of ocean heat uptake under climate change. *Journal of Climate*, *27*(22), 8444–8465. https://doi.org/10.1175/jcli-d-13-00344.1

Masson, D. (1991). Wave-induced drift force in the marginal ice zone. *Journal of Physical Oceanography*, *21*(1), 3–10. https://doi.org/10.1175/1520-0485(1991)021<0003:WIDFIT>2.0.CO;2

Montiel, F., Squire, V. A., & Bennetts, L. G. (2016). Attenuation and directional spreading of ocean wave spectra in the marginal ice zone. *Journal of Fluid Mechanics*, *790*, 492–522. https://doi.org/10.1017/jfm.2016.21

Rogers, W. E., Thomson, J., Shen, H. H., Doble, M. J., Wadhams, P., & Cheng, S. (2016). Dissipation of wind waves by pancake and frazil ice in the autumn Beaufort sea. *Journal of Geophysical Research*, *121*, 7991–8007. https://doi.org/10.1002/2016JC012251

Sentinel-1, T. (2013). *Sentinel-1 user handbook* (Tech. Rep. GMES-S1OP-EOPG-TN-13-0001). Frascati, Italy: European Space Research Institute (ESRIN).

Shen, H., Perrie, W., Hu, Y., & He, Y. (2018). Remote sensing of waves propagating in the marginal ice zone by SAR. *Journal of Geophysical Research: Oceans*, *123*, 189–200. https://doi.org/10.1002/2017JC013148

Shulz-Stellenfleth, J., & Lehner, S. (2002). Spaceborne synthetic aperture radar observations of ocean waves traveling into sea ice. *Journal of Geophysical Research*, *107*(C8), 3106. https://doi.org/10.1029/2001JC000837

Smith, M., Stammerjohn, S., Persson, O., Rainville, L., Liu, G., Perrie, W., et al. (2018). Episodic reversal of autumn ice advance caused by release of ocean heat in the Beaufort sea. *Journal of Geophysical Research: Oceans*. https://doi.org/10.1002/2018JC013764

Squire, V. (2007). Of ocean waves and sea-ice revisited. *Cold Regions Science and Technology*, *49*(2), 110–133. https://doi.org/10.1016/j.coldregions.2007.04.007

Stopa, J. E., Ardhuin, F., Chapron, B., & Collard, F. (2015). Estimating wave orbital velocity through the azimuth cutoff from space-borne satellites. *Journal of Geophysical Research: Oceans*, *120*, 7616–7634. https://doi.org/10.1002/2015JC011275

Stopa, J. E., Ardhuin, F., & Girard-Ardhuin, F. (2016). Wave climate in the arctic 1992–2014: Seasonality and trends. *The Cryosphere*, *10*(4), 1605–1629. https://doi.org/10.5194/tc-10-1605-2016

Stopa, J. E., Sutherland, P., & Ardhuin, F. (2018). Strong and highly variable push of ocean waves on southern ocean sea ice. *Proceedings of the National Academy of Sciences of the United States of America*. https://doi.org/10.1073/pnas.1802011115

Stroeve, J., Holland, M. M., Meier, W., Scambos, T., & Serreze, M. (2007). Arctic sea ice decline: Faster than forecast. *Geophysical Research Letters*, *34*, L09501. https://doi.org/10.1029/2007GL029703

Sutherland, G., Halsne, T., Rabault, J., & Jensen, A. (2017). The attenuation of monochromatic surface waves due to the presence of an inextensible cover. *Wave Motion*, *68*, 88–96. https://doi.org/10.1016/j.wavemoti.2016.09.004

Thomson, J. (2012). Wave breaking dissipation observed with "SWIFT" drifters. *Journal of Atmospheric and Oceanic Technology*, *29*(12), 1866–1882. https://doi.org/10.1175/jtech-d-12-00018.1

Thomson, J. (2015). *Onr sea state dri cruise report R/V Sikuliaq, fall 2015* (SKQ201512S). Seattle, WA: University of Washington.

Thomson, J., Ackley, S., Shen, H. H., & Rogers, W. E. (2017). The balance of ice, waves, and winds in the arctic autumn. *EOS*, *98*, 30–34. https://doi.org/10.1029/2017EO066029

Thomson, J., Fan, Y., Stammerjohn, S., Stopa, Rogers, W. E., Girard-Ardhuin, F., Ardhuin, F., et al. (2016). Emerging trends in the sea state of the Beaufort and Chukchi seas. *Ocean Modelling*, *105*, 1–12. https://doi.org/10.1016/j.ocemod.2016.02.009

Turner, J., Bracegirdle, T. J., Phillips, T., Marshall, G. J., & Hosking, J. S. (2013). An initial assessment of Antarctic sea ice extent in the cmip5 models. *Journal of Climate*, *26*(5), 1473–1484. https://doi.org/10.1175/jcli-d-12-00068.1

Wadhams, P., Squire, V. A., Goodman, D. J., Cowan, A. M., & Moore, S. C. (1988). The attenuation rates of ocean waves in the marginal ice zone. *Journal of Geophysical Research*, *93*(C6), 6799–6818. https://doi.org/10.1029/JC093iC06p06799